Multiple-Scale Variations of Wind-Generated Waves in the Southern California Bight

Cao, Yuhan
Dong, Changming
Uchiyama, Yusuke
Wang, Jin
Yin, Xunqiang

(Citation)
Journal of Geophysical Research: Oceans,123(12):9340-9356

(Issue Date)
2018-12

(Resource Type)
journal article

(Version)
Version of Record

(URL)
https://hdl.handle.net/20.500.14094/90006809

Journal of Geophysical Research: Oceans

RESEARCH ARTICLE
10.1029/2018JC014505

Multiple-Scale Variations of Wind-Generated Waves in the Southern California Bight

Yuhan Cao[1], Changming Dong[1,2], Yusuke Uchiyama[3], Jin Wang[1], and Xunqiang Yin[4]

[1]Oceanic Modeling and Observation Laboratory, School of Marine Sciences, Nanjing University of Information Science and Technology, Nanjing, China, [2]Department of Atmosphere and Oceanic Sciences, University of California, Los Angeles, CA, USA, [3]Department of Civil Engineering, Kobe University, Kobe, Japan, [4]The First Institute of Oceanography, State Oceanic Administration, Qingdao, China

Key Points:
- A numerical wave model is integrated for 10 years to study the wind-generated waves in the SCB
- The analysis of the model results and the observational data shows that the wind-generated waves in the SCB vary in multiple temporal scales
- Effects of currents and topography on waves in the SCB are investigated

Correspondence to:
C. Dong,
cmdong@nuist.edu.cn

Citation:
Cao, Y., Dong, C., Uchiyama, Y., Wang, J., & Yin, X. (2018). Multiple-scale variations of wind-generated waves in the Southern California Bight. *Journal of Geophysical Research: Oceans*, *123*, 9340–9356. https://doi.org/10.1029/2018JC014505

Received 22 AUG 2018
Accepted 6 DEC 2018
Accepted article online 9 DEC 2018
Published online 26 DEC 2018
Corrected 29 JAN 2019

This article was corrected on 29 JAN 2019. See the end of the full text for details.

Abstract A numerical wave model is applied to study the wind-generated wave in the Southern California Bight (SCB). Observational data available in this area are used to validate the numerical model results. The model is integrated for 10 years (2004–2013). The comparison of the model results with observations shows that the model well reproduces the wave variations in the SCB. The multiple-scale variations in the wavefield are examined: interannual, seasonal, intraseasonal, and diurnal. The significant wave height and swell wave height distributions display distinct patterns during different seasons. On the interannual scale, the wave variation in the SCB is influenced by El Niño–Southern Oscillation activities. Intraseasonal scale events occur frequently. Land/sea breezes cause the diurnal variation. The effects of topography (especially islands) and currents on waves are analyzed. The islands in the SCB provide significant sheltering effects to the coast from deep-ocean waves. The effect of background currents on waves is discussed.

Plain Language Summary A numerical model is used to simulate the wind waves in the Southern California Bight (SCB). The analysis of the model results together with the observational data show that the wind waves in the SCB vary from season to season, from year to year, events with periods from a few days to tens of days happen frequently, and waves near the coast change directions in 24 hr. The effects of currents and topography on the waves are discussed.

1. Introduction

The wind-generated wave plays an important role in the air-sea interaction. Investigation of multiple-scale variations can help us to better understand physical processes in the Southern California Bight (SCB). The wind-generated wave plays an important role in the air-sea interaction. Investigation of multiple-scale variations can help us to better understand physical processes in the SCB.

The SCB lies on the west coast of the United States, which features a particularly complex shelf configuration of tectonic origin. Numerous offshore islands and shallow banks in the bight provide significant shelter to the coast from deep ocean waves. The bight extends from approximately 32°N to Point Conception at 34.5°N shown in Figure 1, in which eight islands are presented: Santa Rosa, San Miguel, Anacapa, and Santa Cruz islands fringing the Santa Barbara Channel, Santa Catalina Island near the Palos Verdes Peninsula, and San Clemente, Santa Barbara, and San Nicolas islands far offshore. The water depth is the deepest in the southwest and decreases steeply around the islands and near the coast. Wave climate in the region is affected by the prevailing northwest winds along the California coast, tropical storms, and swell propagating from the west and northwest, with associated wave refraction and diffraction (Adams et al., 2008; Arthur & Siple, 1951; Dong et al., 2009; O'Reilly et al., 1999; O'Reilly & Guza, 1993; Pawka et al., 1984). The sea surface wave plays an important role in the air-sea exchange, such as the momentum and carbon dioxide exchanges. The wave includes two parts: the local wind-driven wave and the swell propagating from the remote wind wave. Due to the variation of the wind and effects of wave propagation, both the two types of waves carry multiple-scale variations. Investigation of multiple-scale variations can help us to better understand wave dynamics in the SCB, which is not well documented in literature. The knowledge of multiple-scale variation in the wind-generated wave is necessary in variety of applications including sediment transports, coastal erosion, design of coastal constructions, and pollution transports.

The study of the variability and dynamic processes of waves in the California coasts including the SCB has been reported in literature. Seymour (1996) reports that wave height increases during westerly storm

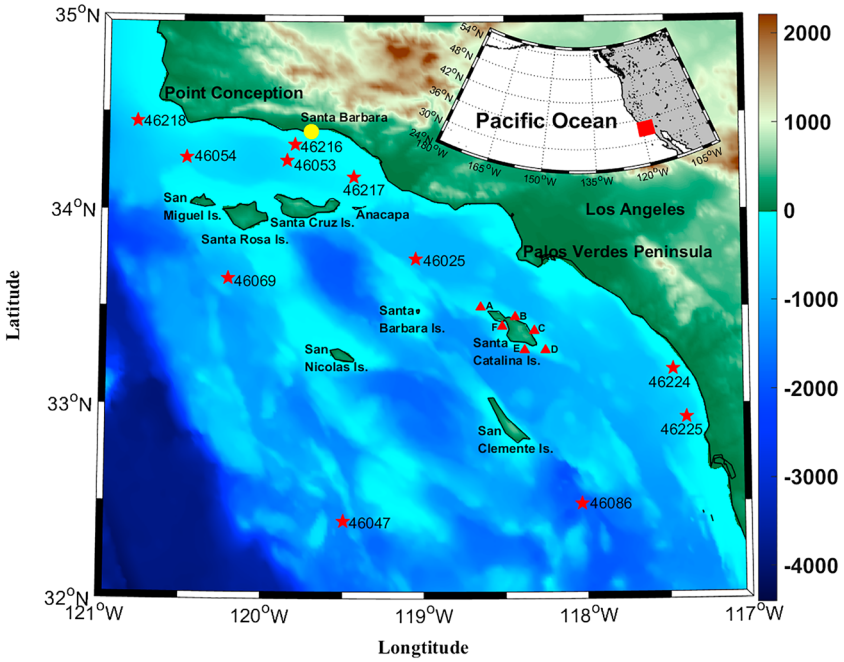

Figure 1. Simulation domain. Shaded is the bathymetry (unit: m) from ETOPO1. The red five-pointed stars and yellow circle represent buoy stations and the red triangles represent the location of the selected model experiment points. The yellow dot in the Santa Barbara Channel is the site for the test of diurnal variation. Inset map of northeastern Pacific Ocean shows location of the Southern California Bight (SCB).

events associated with El Niño phases. Eshleman et al. (2005) uses the Simulating WAves Nearshore (SWAN) model (Booij et al., 1999) to simulate the wave process off San Francisco, California, and analyzes the effect of beach shape variations on wave energy. Rogers et al. (2007) numerically simulate the SCB wind waves using the SWAN model and propose that the sheltering effects are important. Adams et al. (2008) examine the historic wave climate events in the deep water of the Southern California and its relationship with the El Niño–Southern Oscillation (ENSO) events. Xu and Noble (2009) analyze wave data from 18 buoys in the SCB to characterize the spatial and temporal variability of the regional wave climate and point out that Point Conception shelters most of the Bight from being directly impacted by the North Pacific weather. Inside the Santa Barbara Channel, wave heights are commonly only a quarter to half of those in the open ocean. Adams et al. (2011) combine the SWAN model with the Coastal Geomorphic Erosion Model to explore the sensitivity of longshore sediment transport patterns to changes in deep-water wave direction. The numerical models are based on practical boundary conditions to estimate monitoring and prediction of waves in the SCB (Crosby et al., 2016; O'Reilly et al., 2016). Driven by the variations of atmospheric forcing with the complex bathymetry in the SCB, the oceanic circulation in the area possesses multiple-scale variation suggested by Dong et al. (2009), which implies the possibility of existence of the same multiple-scale variability in the wind-generate wavefield. However, the latter topic has not been reported in literature.

The present study applies a high-resolution wave model to analyze the multiple-scale variability of surface wave in the SCB. This paper is organized as follows: the data used in the study is described in section 2. In section 3, the model configuration is introduced. Section 4 is the model results including the analysis of the interannual, seasonal, intraseasonal, and diurnal variations of the SCB wavefields during the 10 years (2004–2013). Sheltering effects of islands and current influences on waves are discussed in section 5, and the summary is presented in section 6.

2. Model Configuration

The SWAN model version 41.10 (Booij et al., 1999, 2001) is used to simulate the wave dynamics in the SCB. Its governing equation in a spherical coordinate is based on the spectral action balance equation given as follows:

Table 1
Configurations of the Simulating WAves Nearshore Model

Parameter	Value/scheme
Time step (min)	5
Number of meshes in θ space	24
Lowest discrete frequency (Hz)	0.0418
Highest discrete frequency (Hz)	1
Physics process	GEN3 JANSSEN (Cavaleri and Malanotte-Rizzoli 1981)
Shape of the spectra	JONSWAP
Propagation scheme	Backward Space Backward Time (BSBT)
Spatial resolution (km)	2 × 2
Temporal resolution (hr)	1
Coordinate	Spherical
Mode	Nonstationary 2-D mode

$$\frac{\partial N}{\partial t}+\frac{\partial c_\lambda N}{\partial \lambda}+\frac{\partial c_\varphi N}{\partial \varphi}+\frac{\partial c_\sigma N}{\partial \sigma}+\frac{\partial c_\theta N}{\partial \theta}=\frac{S_{tot}}{\sigma} \quad (1)$$

where N is the action density with respect to longitude λ and latitude φ, σ is the relative radian frequency, θ is the wave propagation direction, c_λ, c_φ are the propagation velocities of the wave energy in geographic space, and c_σ, c_θ are the propagation velocities in the spectral σ and θ spaces. It is noted that the advection by the ambient current is not included on the right side of the equation, but its effect on the wave is discussed in section 5. The source term S_{tot} is represented as

$$S_{\mathrm{tot}}=S_{\mathrm{in}}+S_{\mathrm{nl3}}+S_{\mathrm{nl4}}+S_{\mathrm{ds},w}+S_{\mathrm{ds},b}+S_{\mathrm{ds,br}} \quad (2)$$

where S_{in} is the wind-generated energy input, S_{nl3} and S_{nl4} are triplet and quadruplet wave-wave interactions, respectively, $S_{\mathrm{ds},w}$ is the dissipation by the white capping, $S_{\mathrm{ds},b}$ is the dissipation by the depth-induced wave breaking, and $S_{\mathrm{ds,br}}$ is the dissipation by the bottom friction. In the model, the transfer of wind energy to the waves is described by a resonance mechanism (Phillips, 1957) and a feedback mechanism (Miles, 1960). Both linear and exponential wind input growths are included in the model. The whitecapping formulations are based on a pulse-based model (Hasselmann, 1974), as adapted by the WAMDI group (Hasselmann et al., 1988). The bottom friction models selected for the SWAN are the empirical model of JONSWAP (Hasselmann, 1973) form with a friction coefficient of C_{bottom} = 0.067 m^2/s^3, the drag law model of Collins (1972), and the eddy-viscosity model of Madsen et al. (1988). For the energy dissipation in random waves due to depth-induced breaking, the bore-based model of Battjes and Janssen (1978) is used. Quadruplet (deep water) and triad-wave (shallow water) interactions are activated using the default settings for the Discrete Interaction Approximation (DIA) (Hasselmann et al., 1985) and the Lumped Triad Approximation (LTA). In the SWAN, a partially modeled diffraction is added to the model using a phase-decoupled refraction diffraction approach (Holthuijsen et al., 2003).

The parameters and configurations used in the SWAN are listed in Table 1. An unsteady two-dimensional calculation mode is adopted with the grid defined on a spherical coordinate system between latitudes 32°–35°N and longitudes 117°–121°W. The model is started from a rest state and assumes constant values at times after the end of each input parameter. The extra 3-day model simulation prior to the designed period is conducted for the initial condition. The model is run for 10 years from 1 January 2004 to 31 December 2013.

2.1. Bathymetry Data

Bathymetric data used for the present wave model is from ETOPO1 (Amante & Eakins, 2009), provided from the National Oceanic and Atmospheric Administration (NOAA), which is a 1-arc min global relief model of the Earth's surface that integrates land topography and ocean bathymetry. In other words, it represents a spatial resolution of 0.0167° × 0.0167°.

2.2. Atmospheric Forcing

An hourly sampled Weather Research and Forecasting Model (WRF) 10-m wind field data with 6 km in horizontal resolution for 10 years from 2004 to 2013 are used to drive the SWAN. The domain of the input wind is larger than the computational one, which is between latitudes 25°–40°N and longitudes 110°–130°W. The WRF product has been validated against observational data, and the details can be found in Renault et al. (2016).

2.3. Lateral Boundary Conditions

For the boundary conditions, six-hourly significant wave height of combined wind waves and swell, mean wave direction, and mean wave period of the ERA-Interim reanalysis data, which are provided by the European Centre Medium-Range Weather Forecasts, are used for the SWAN model. In the model, the JONSWAP spectrum is used as the shape of the spectra (both in frequency and direction) at the boundary of the computational grid in the case of parametric spectral input. The peak enhancement parameter of the spectrum is set as default value. The parametric spectra at the boundary are defined, which consist of

Table 2
Information of Buoy Data in the Simulation Area

No.	Long. (°W)	Lat. (°N)	Missing data (H_{sign})	Observation numbers (H_{sign})	Missing data (MWD)	Observation numbers (MWD)
46025	119.1	33.7	7%	80,766	46%	47,239
46047	119.5	32.4	19%	70,925	51%	42,843
46053	119.9	34.2	6%	82,155	38%	54,094
46054	120.5	34.3	32%	58,962	99%	529
46069	120.2	33.6	21%	68,515	38%	53,904
46086	118.0	32.5	9%	79,226	19%	70,482
46216	119.8	34.3	9%	79,253	42%	50,688
46217	119.4	34.2	11%	77,262	43%	49,235
46218	120.8	34.4	18%	71,284	44%	48904
46224	117.5	33.2	10%	78,283	43%	49,800
46225	117.4	32.9	10%	78,590	42%	50,586

Note. MWD = mean wave direction.

two parts, the first part defines the boundary segments where the spectra are given and the second part defines the spectral parameters of these spectra. The ERA-Interim reanalysis data (Dee et al., 2011) assimilates ocean wave height data derived from spaceborne radar altimeters into the wave model. Parametric wave quantities of ERA-Interim are based on the Wave Modeling approach (Komen et al., 1994). A four-dimensional variational data assimilation scheme is used in ERA-Interim. The ERA-Interim provides a variety of products with different spatial resolutions from 0.125° to 3°. For the current study, the highest one with the resolution of 0.125 ° is selected.

3. Observational Data and Model Validation

Validation of the model result for significant wave height (H_{sign}) and mean wave direction (MWD) is conducted by using hourly observational H_{sign} and MWD data from 11 National Data Buoy Center buoys in the SCB (Figure 1) over the 2004–2013 period. The average number of null values of the measured wave height data from 11 buoys is about 13%. The detailed information on the wave measurements at these stations is listed in Table 2.

The observed H_{sign} is calculated by taking the average of the highest one third of all wave heights during a 20-min sampling period. The directions of waves at the dominant period are coming which measured in degrees, increasing clockwise with the northward one as 0° and the eastward one as 90°. The correlation coefficients between the hourly SWAN data and buoy observations are between 0.50 and 0.67. The mean H_{sign} and the MWD of the simulated and observed data at 11 stations are 1.46 (276.62°) and 1.50 m (262.32°), respectively. The relative errors of mean simulated H_{sign} and MWD are 2.4% and 5.4%, respectively. The mean standard deviation (STD $= \left(\frac{1}{n}\Sigma_{i=1}^{n}(x_i-\overline{x})^2\right)^{\frac{1}{2}}$, $\overline{x}=\frac{1}{n}\Sigma_{i=1}^{n}x_i$, where n is the number of elements in the sample and x is a data vector) of the simulated and observed H_{sign} at 11 stations are 0.63 and 0.58 m, respectively. The relative error of mean STD of simulated H_{sign} is 7.9%.

Figure 2 displays the means and STDs of observed and modeled H_{sign} and MWD at the individual 11 stations. At Station 46054, the mean observed H_{sign} is 1.95 m and the mean modeled one is 1.96 m. The STDs of observed and modeled are 0.77 and 0.71, respectively. At Station 46053, both the mean observed and modeled H_{sign} are 1.24 m. The STDs of observed and modeled are 0.51 and 0.58, respectively. At Station 46047, the mean observed H_{sign} is 2.10 m and the mean modeled one is 2.00 m. The STDs of observed and modeled are 0.83 and 0.74, respectively. At Stations 46054, 46053, and 46047, the mean observed (modeled) MWDs are 290.0° (296.6°), 269.8° (272.7°), and 292.3° (300.9°), respectively. The STDs of observed (modeled) MWD at the three stations are 29.1 (26.1), 22.6 (36.4), and 39.0 (30.2), respectively. The above numbers suggest that the SWAN model well reproduces H_{sign} and MWD in the SCB.

4. Results

In this section, the multiple-scale variations of the waves in the SCB are examined using the SWAN data: interannual, seasonal intraseasonal, and diurnal. Before discussing the temporal variation, we present 10-year mean states of sea surface wind, significant wave height, swell wave height, and peak wave period, shown in Figure 3. Mean wind speed $|\mathbf{U}|$ (Figure 3a) is calculated using the zonal (U_i) and meridional (V_i) components of wind as

$$|\mathbf{U}| = \frac{1}{n}\Sigma_{i=1}^{n}\sqrt{U_i^2+V_i^2} \tag{3}$$

where i represents the hourly time step and n is the total number of hours during periods from 2004 to 2013. The mean wind speed for the SCB is between 3 m/s and 9 m/s, with the highest in the open sea and the area near Point Conception in the SCB, the wind speed decrease dramatically from offshore to nearshore. The wind direction over the SCB is predominantly from the northwest. Figure 3b shows relatively large H_{sign} in

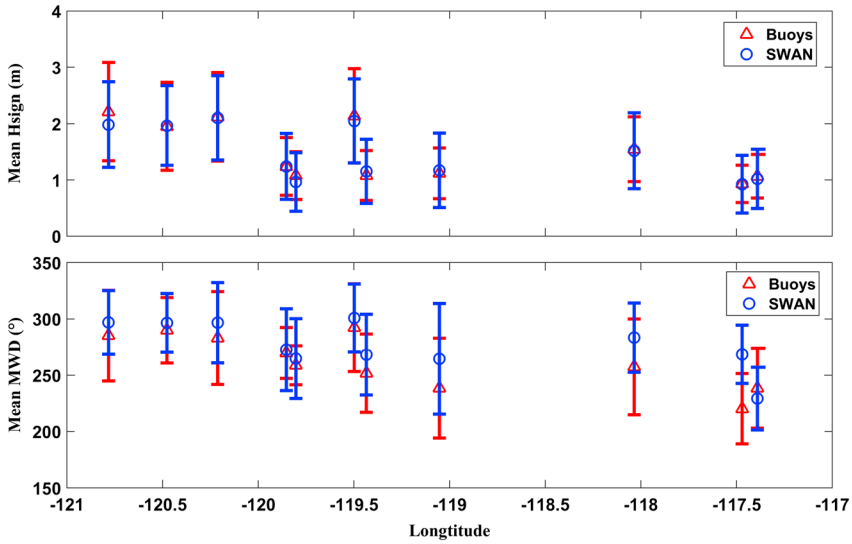

Figure 2. Significant wave height comparisons between National Data Buoy Center and Simulating WAves Nearshore (SWAN) for 2004–2013. The blue circles and red triangles represent, respectively, the SWAN data and measured significant wave height at each buoy location. The blue and red error bars represent, respectively, the standard deviation of SWAN and measured significant wave height. The mean bias is smaller than 0.3 m. There is a good agreement between SWAN and observation data. MWD = mean wave direction.

the southwest part of the SCB ranging from 2 to 2.5 m. The distribution of the wavefield is basically consistent with that of the local wind field. In the nearshore areas, H_{sign} is relatively small ranging from 0.5 m to 1 m. H_{sign} is also observed to gradually decrease from 2 m in the deep ocean to 0.5 m near the shore. Additionally,

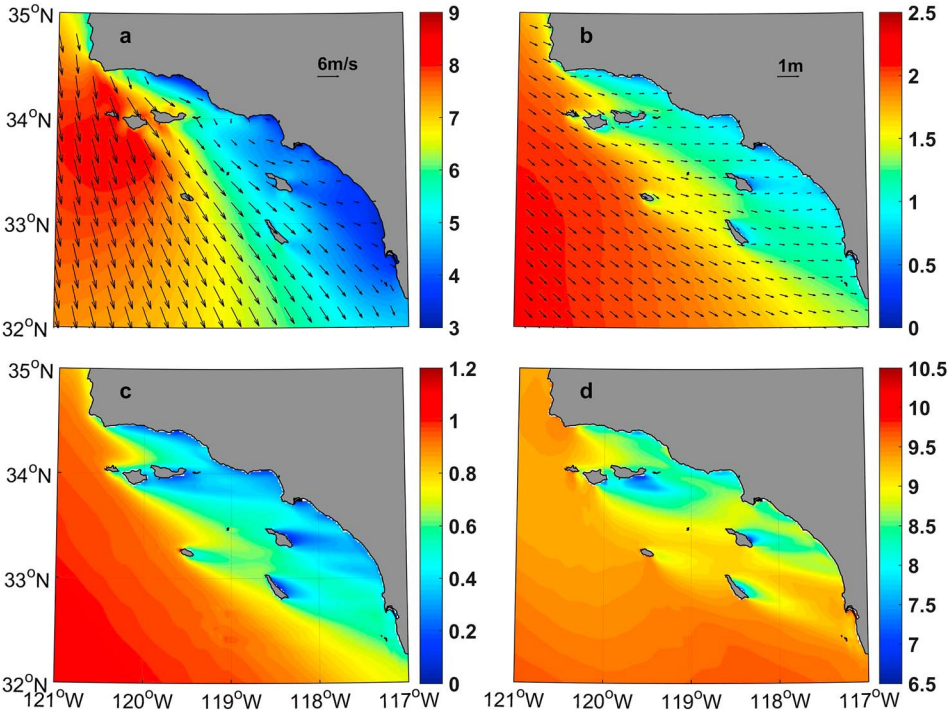

Figure 3. Ten-year average (2004–2013) distribution of 10-m wind, significant wave height, swell wave height, and peak period in the Southern California Bight. (a) Ten-meter winds (vectors; unit: m/s) and wind speed (color shadings, unit: /s); (b) significant wave height (shade; unit: m) and mean wave direction (vector); (c) swell wave height (color shadings, unit:); (d) peak period (color shadings, unit: s).

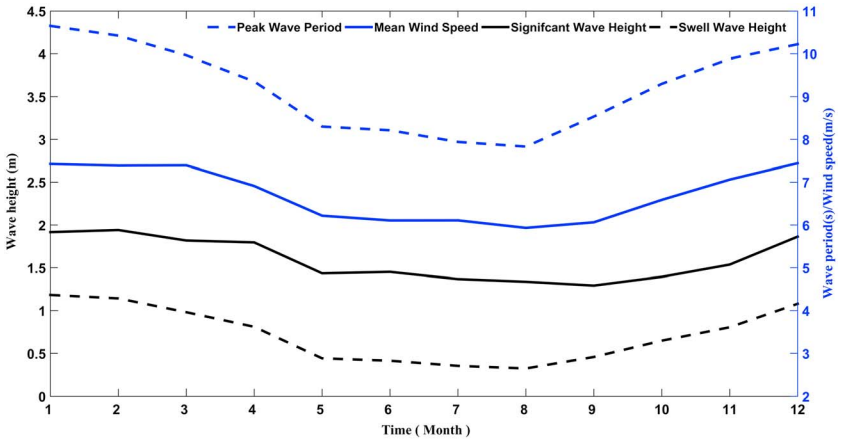

Figure 4. Monthly averages of mean wind speed in the lager domain (blue solid line, unit: m/s), peak wave period (blue dotted line, unit: s), significant wave height (black solid line, unit: m), and swell wave height (black dotted line, unit: m) for 2004 to 2013.

waves in the southeastern side of the islands exhibit a further decrease in the wave height. Wave height on the upwind side relative to the islands is approximately twice as large as that on the lee side of the islands. The direction of wave propagation (see in Figure 3b) is generally southeastward in deep water and eastward in shallow water. The change of wave direction in the nearshore is mainly due to the bathymetric refraction of waves.

Figure 3c shows the time-averaged spatial distribution of swell wave height ($H_{swell} = 4\sqrt{\int_0^{\omega_{swell}}\int_0^{2\pi}E(\omega,\theta)d\omega d\theta}$, where$\omega_{swell} = 2\pi f_{swell}$, E is the variance density spectrum, and $f_{swell} = 0.1$ Hz by default). The general pattern of the spatial distribution of the H_{swell} is similar to that of the H_{sign} in the whole SCB, but in the lee sides of islands, the spatial distribution of the H_{swell} is more significantly affected by the islands than that of H_{sign}. It is easy to see from the figure, the sheltered area of the swell is larger than the mixed wave (Figure 3b) in the SCB, especially, the wavefield in the lee side of Santa Catalina Island. The remotely generated wave energy propagating into the bight is dissipated by the wave breaking and diffraction near the offshore islands (O'Reilly & Guza, 1993). The upwave from the island is blocked from propagating to the sheltered region. The wave at the sheltered region can be reconstructed by adding the wave information that does arrive at the point (amplitudes and phases), radiating from the upwave crest. Repeating this reconstruction in the area downwave from the incident crest gives the entire wavefield in this area, including the sheltered area. The local wind-generated wave is the direct response to the wind, which is affected by an island in a limited lee area. These different processes lead to the significant difference between the swell and mixed wave in the lee sides of islands. In the deep area, H_{swell} is 0.8 to 1 m, while H_{swell} in the shallow water is 0.2 to 0.4 m. In the sheltering area of the islands, H_{swell} is only about 0.2 m. Figure 3d shows the time-averaged peak period (PER). It is found that the period is significantly affected by the wind. The period around Point Conception is relatively large, ranging from 9.5 to 10 s. At the southwestern corner of the model domain, the maximum value of the peak period is 10 s. The wind speed near the shore is small, and the peak period is also reduced. In the island sheltering areas, as the wave energy is dissipated, the peak period decreases significantly.

4.1. Seasonal Variation

This section discusses the perennial average and the seasonal distribution of the wave field in the SCB. Figure 4 shows the time series of the perennial averages for wind speed, H_{sign}, H_{swell}, and PER. The perennial average of the wind field and wavefield is obtained by calculating an area average of the 10 years' monthly mean. The area of the wind field covers the larger area, and that of the wave field is the SCB. From the time series, the seasonal characteristics of wave height and peak period are large in winter and

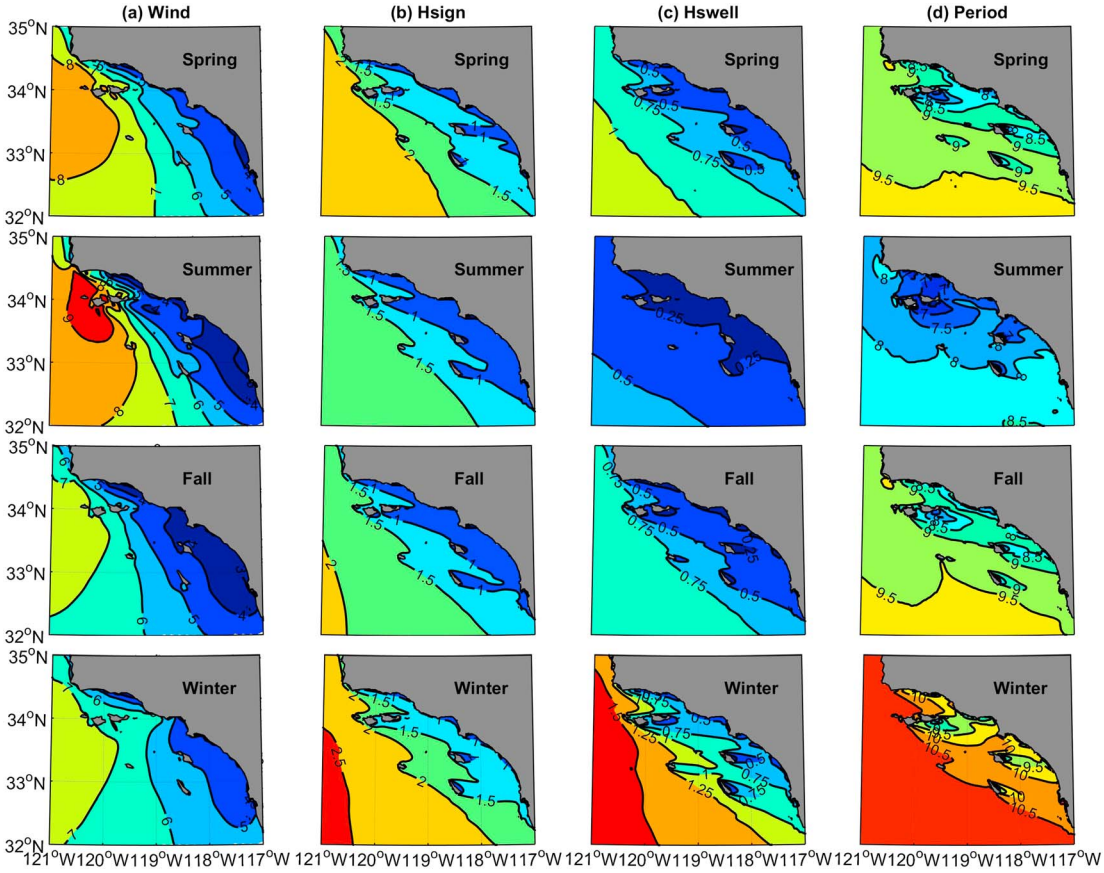

Figure 5. Mean seasonal variations in the Southern California Bight. (a) The 10-m wind speed (unit: m/s), (b) significant wave height, (unit: m), (c) swell wave height, (unit: m), and (d) peak period (unit: s).

small in summer, with the maxima in January and the minima in August. These results are consistent with the seasonality of the wind field (Figure 4). The wind speed is generally the largest in winter and the smallest in summer. The correlation coefficient between the wind speed and H_{sign}, H_{swell}, and the PER are 0.97, 0.98, and 0.97, respectively, with a 95% confidence level. The correlation coefficient shows that the variability of the wavefield in this area is significantly affected by the local wind.

Figure 5 shows the seasonal spatial distribution of the wind and wave fields in the SCB. The four seasons are classified as December–February (winter), March–May (spring), June–August (summer), and September–November (fall). The wind speeds in spring and summer are larger than fall and winter. Wave heights, peak periods are larger in spring and winter than those in fall and summer. In summer, wind speed reaches 9 m/s near Point Conception, but in other offshore areas, the wind speed is much lower, only 3 to 4 m/s, and the wind speed variations on the lee side of the island occur more significantly than those in other areas. The minimum H_{sign} is 0.25 m. The nearshore H_{swell} is 0.25 m. The minimum peak period of 7 s is noted in the sheltered areas of the islands in the SCB. In winter, the maximum wind speed is 7 m/s and the minimum wind speed is 4.5 m/s. The maximum H_{sign} is 2.5 m, which is mainly distributed in the southwest corner of the study area. The H_{sign} is mostly 2 m, which is mainly distributed in coastal areas and island shelters. The maximum H_{swell} is 1.5 m. In the leeward region of the island, the gradient of wave height is large. The PER is 10.5 s, which is mainly distributed in the deep water and the area near Point Conception.

4.2. Interannual Variation

Figure 6 shows the annually averaged time series of sea surface wind speed and wave field in the SCB. It is found that the variation of H_{sign} resembles that of the wind speed. The correlation coefficient between the wind speed and H_{sign} is 0.73. In 2005, the wave height and period are large. Afterward, the wave height

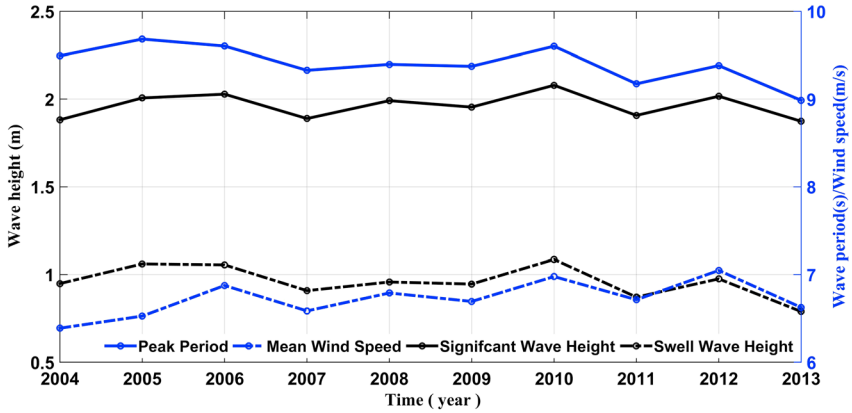

Figure 6. Time series of annual mean of the wind speed (unit: m/s; blue dotted line), significant wave height (unit: m; black line), mean period (unit: s; blue line), and swell wave height (unit: m; black dotted line) in the Southern California Bight between 2004 and 2013.

and period decrease to smaller values in 2007. The wave height and period begin to increase again, reaching the largest in 2010. The wind speed has a similar oscillation during this period.

Waves modulate energy fluxes across the air-sea interface and into the upper ocean, thereby playing important roles in air-sea interaction processes (Young et al., 2011). ENSO is an irregular periodic variation in sea surface temperatures and winds over the tropical eastern Pacific Ocean, affecting the Pacific basin-scale climate change. In order to explore the relationship between ENSO and the wave height, the characteristics of the interannual variation of the wave field in the SCB are analyzed to be related to the ENSO index (Niño3.4 index) during 2004–2013. The Niño3.4 index (Saha et al., 2017) is defined as sea surface temperature anomalies in the Niño 3.4 region (5°S–5°N, 170°–120°W), which has been obtained from the website: http://www.cpc.ncep.noaa.gov/data/indices. In 2009–2010 (Yuan et al., 2012), a relatively strong El Niño event occurs when the Niño3.4 index is largest during the 10 years.

To further investigate the relationship of the waves in the SCB with the ENSO, we apply a low-pass filter to remove the seasonal signals from the monthly H_{sign} and Niño 3.4 index (Figure 7). In 2010 when the El Niño event happens, the trade winds become weaker, which implies the weakening of the whole subtropical atmospheric circulation near the sea surface, including the SCB area. Usually weak wind drives low wave

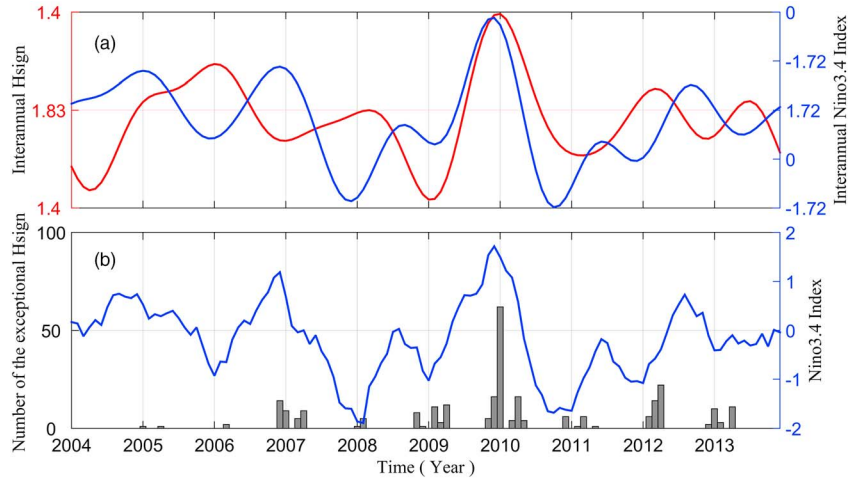

Figure 7. (a) The interannual variability of significant wave height and Niño 3.4 index. The left ordinate represents the annual average of the H_{sign} (without the seasonal signal), and the right represents Niño 3.4 index (without the seasonal signal). The red solid lines represent model data and the blue solid lines represent Niño3.4 index. (b) The number of the month exceptional H_{sign} at station 46225 compared with the Niño3.4 index.

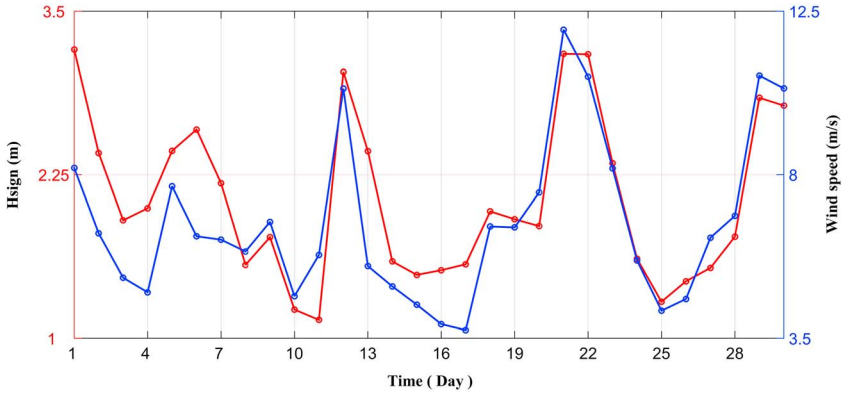

Figure 8. Time series of daily averaged significant wave height (red line) and wind speed (blue line) during April 2010. The correlation between wind speed and H_{sign} reaches 0.83.

height, however, as we see from Figure 7a that the wave heights are the largest in the 10 years. The cause of the strong wave in the ENSO year is considered as high frequency of storm occurrence (Adams et al., 2008; Seymour et al., 1985; Storlazzi & Griggs, 2000). From the observations at the buoy stations are relatively complete. Figure 7b shows that there are more large wave events in 2010 than other years at Station 46225.

4.3. Intraseasonal Variation

This subsection mainly analyzes the intraseasonal variability of H_{sign}. As an example, Figure 8 shows the daily time series of H_{sign} and average wind speed in April 2010. A strong correlation of 0.83 exists between wind speed and H_{sign}, which shows that the wind field within 1 month has a great impact on the wavefield. The wind field and wave field share an oscillation period of about 7 days. Figure 9 shows that both the wind and wave spatial distributions have clear similar patterns between 23 and 29 April 2010 with a repeating pattern of decrease and increase. From the figure, it can be seen that along most of the coastal areas, both wave heights and wind speeds are small. On 23 April, both wave heights and wind speeds exhibit large values in most of the SCB, the wave height and wind speed decrease to small values on 25 April 25, and afterward, the wave height and wind speed begin to increase again.

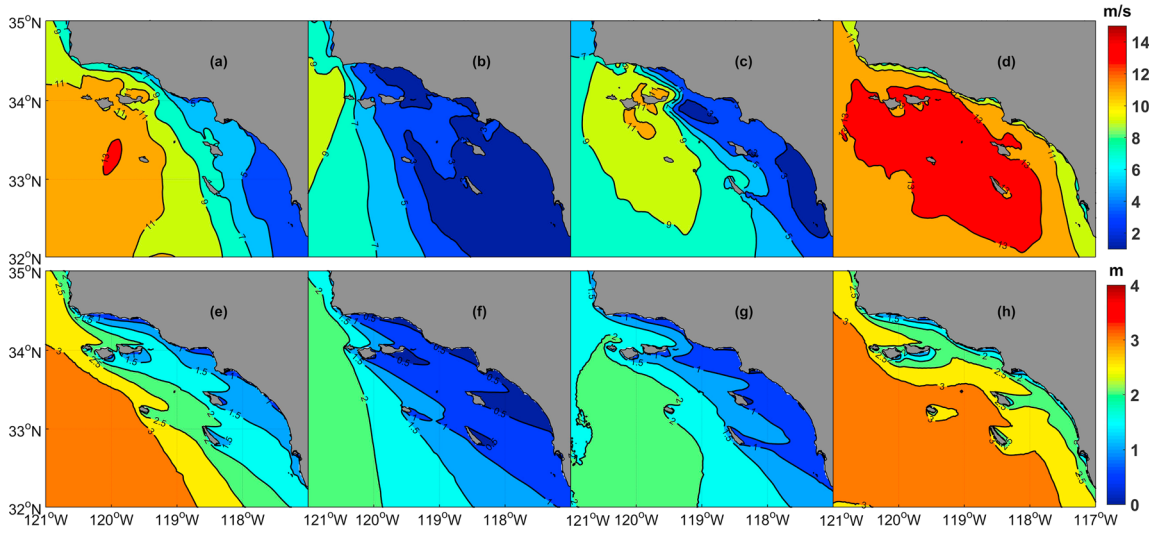

Figure 9. Temporal variations of daily-averaged wind speed (m/s) and significant wave height (m) in April 2010. (a–h) For 23–29 April 2010, (a and e) for 23 April, (b and f) for 25 April, (c and g) for 27 April, and (d and h) for 29 April.

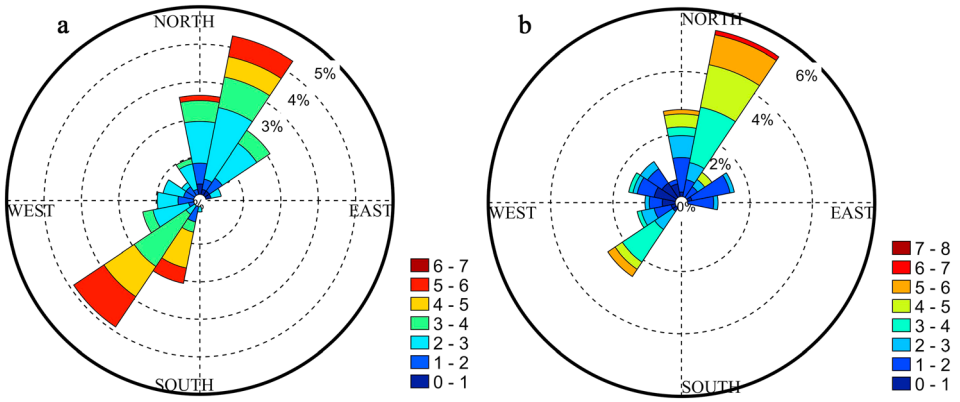

Figure 10. Wind rose on 25–27 July 2010 (a) and 27–29 August 27-29, 2010 (b) at Santa Barbara buoy station. The range of wind speed (unit: m/s) is represented by the different colors shown in the legend.

4.4. Diurnal Variation

While the California Current is a persistent cold southward current flowing through the SCB accompanied by the northward countercurrent close to the shore, diurnally fluctuating flows are also quite substantial. Because of existence of the deserts in Southern California, the coastal land-sea breeze is pronounced during boreal summer that is speculated to influence on flows and waves at the diurnal frequency. Hughes et al. (2007) use observational data to analyze the diurnal variations of the wind field near the coast of Southern California during summer and notice a significant diurnal cycle in the direction of the offshore wind. The land-sea breeze systems have a significant impact on the costal wave characteristics (Remya & Kumar, 2013).

To investigate the diurnal variation of waves in the SCB, a wave buoy located in the Santa Barbara Channel, approximately 3 m away from the shore (Figure 1), is used as a case study. Wind roses on 25–27 July 2010 and 25–27 August 2010 are shown in Figure 10. Winds are distributed in multiple directions near the shore, and the wind directions are generally onshore during the day and offshore at night. Furthermore, the wind speeds change greatly between 1 and 7 m/s. Figure 11 shows diurnal variation of the air temperature, wind field, and wavefield during same period in the local time. The air temperature changes between 12 and 17 °C in the two period. The wind speeds vary between 1 and 7 m/s with a diurnal oscillation. It can be seen from Figure 11 that in the high frequency of the variation (diurnal variation), the wave variation is not in the same pace as the wind variation and slightly lags behind the wind variation, which is different from that in the longer time scale, such as intraseasonal, seasonal, and interannual variations (in the longer time scale, wind, and wave variations are in the same pace, see Figures 4, 6, and 8.

In summary, waves in the SCB have a significant seasonal variation: in winter, the H_{sign}, H_{swell}, and PRE are large, and small in summer. In the interannual scale, waves are affected by the ENSO activities. In the intraseasonal scale, winds have a great impact on the waves in the SCB. Sea breeze and land breeze has impacts on the waves in the diurnal scale.

5. Discussion

A capability of wave diffraction in SWAN version 41.10 provides us a great opportunity to realistically describe the propagation process of waves in the nearshore, including areas sheltered by islands and semienclosed basins. In addition, the governing equation of the SWAN model is based on the spectral action balance equation, which represents conservation of spectral wave action density with background currents that interact with waves. Therefore, the SWAN model is suitable to study the influence of current on wave propagation. In this section, sheltering effects of islands and oceanic currents on waves are discussed.

5.1. Sheltering Effects of Islands

Pawka et al. (1984) show that low-frequency waves have a strong refraction effect near the island in the SCB using a numerical model. O'Reilly et al. (1999) use a spectral analysis of buoy data to study the dissipation of wave energy by the reflection from cliffs on the coast of California. Their results show that swells are affected

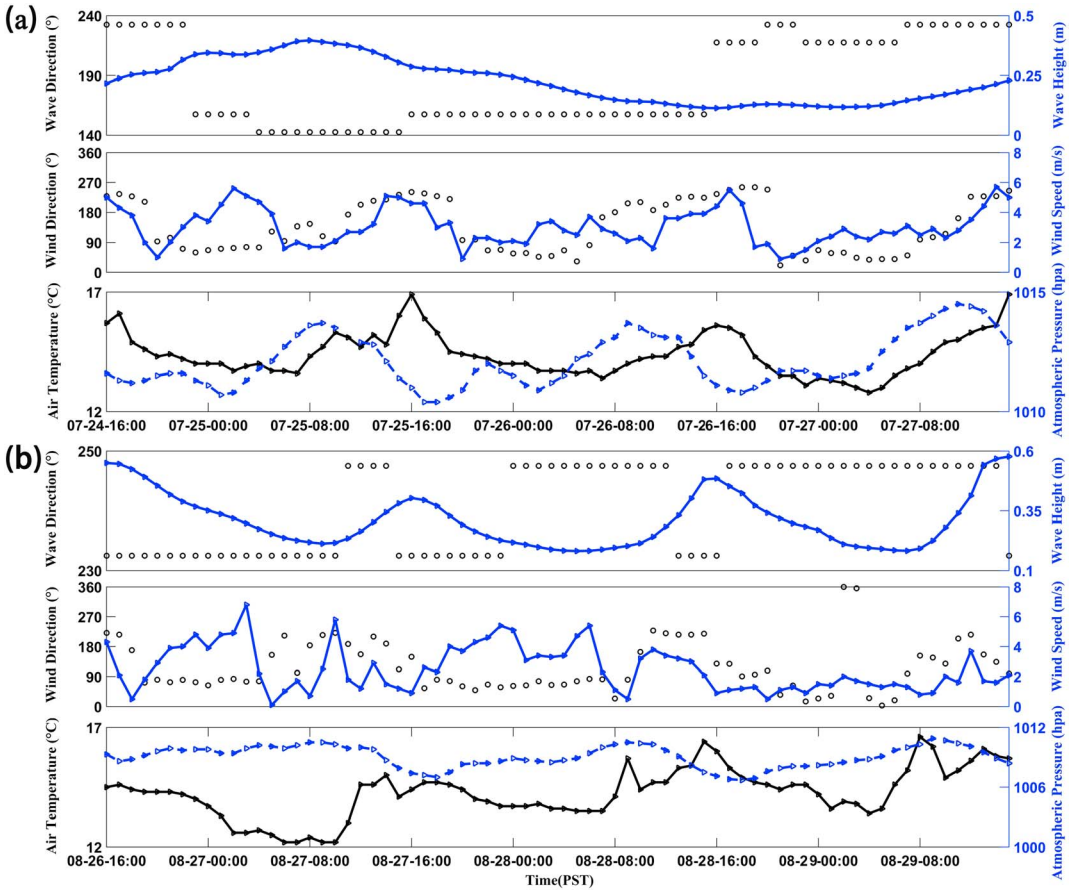

Figure 11. Diurnal variation of winds, waves and air temperature observed by Santa Barbara buoy. The diurnal variation (a) on 24–27 July 2010 and (b) on 26–29 August 2010 in local time.

by the sheltered of Point Conception and the Channel Islands. León and Soares (2005) employ a wave model with a very fine grid to simulate the sheltering effect of the Azores Islands (Portugal) in the North Atlantic Ocean. They find that in strong wind conditions, the sheltering effect of islands is significant. The presence of the Azores Islands induces a spread of energy and changes in the directional wave spectrum while reducing the wave height. León and Soares (2010) find that the islands block the propagation and generation of waves in the lee side that modify the resulting sea states to reduce the significant wave height and to change the peak period. Previous researches have recognized that islands have a significant sheltering effect on coastal areas due to attenuation of surface gravity waves.

In this section, we investigate the influence of the islands in the SCB on wave propagation under high wind conditions. Figure 12 shows an example of the island sheltering effects on wave variables in January for 10 years. When the waves propagate from the northwest, the sheltering effect of the six islands retard the arrival of the significant wave height front to the coast of the continental SCB (Figure 12a). Generally, swells propagate from the northwest to the bight (Figure 12b) and the wave height decreases behind the islands. The spatial distribution of wave direction (Figure 12c) demonstrates that the mean propagation directions are significantly different on both the up and downwind sides of the islands. The peak period (Figure 12d) on the leeward side shows significant reduction.

To discuss the island effects on wave propagation, we choose six points around Santa Catalina Island defined clockwise from the northern tip, as denoted by the red triangles in Figure 1. The rose diagram (Figure 13) of wave directions and heights at the six selected points in January 2011 shows that wave heights greater than 1 m are mostly observed at the Point A, followed by Points E and F on the upstream of the island in terms of wind. At the Points B, C, and D on the leeward side, the wave heights are mostly less than 1 m, especially at

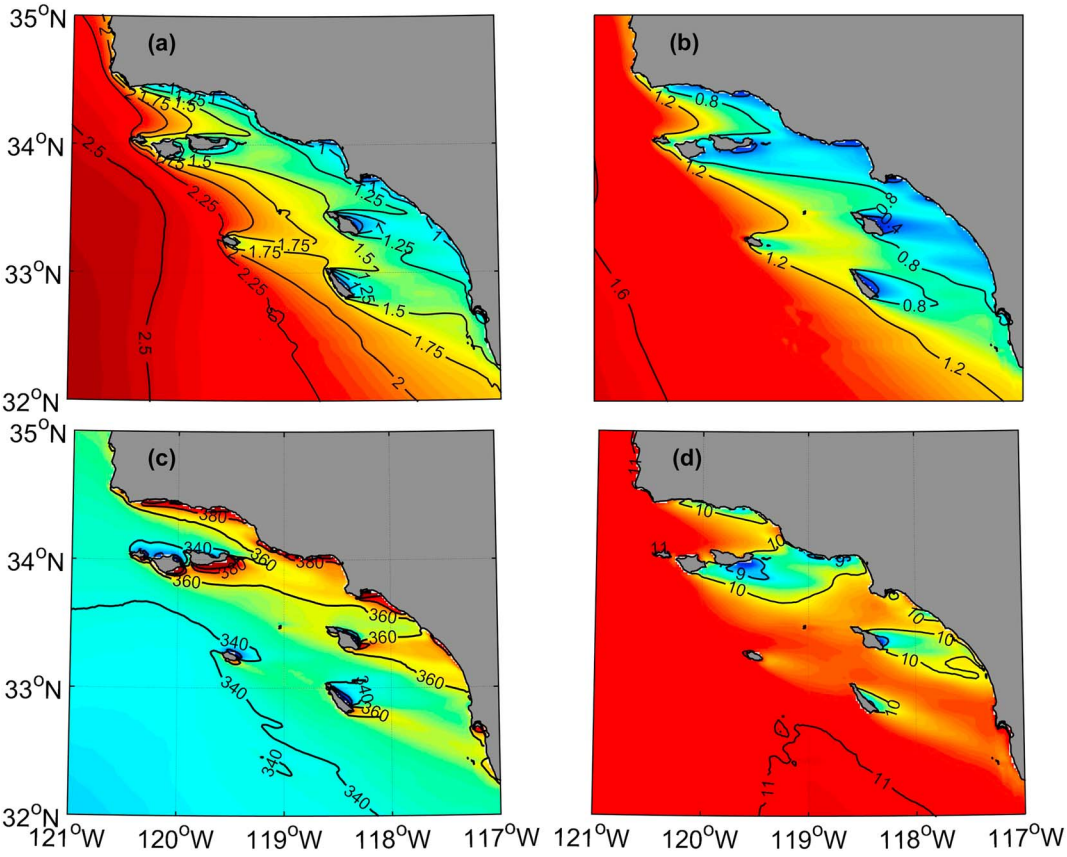

Figure 12. Island sheltering in the Southern California Bight. (a) Significant wave height, (shaded; unit: m); (b) swell wave height, (unit: m); (c) is mean wave direction (unit: °); (d) peak wave period (unit: s). Panels are for indicated variables in January from 2004 to 2013.

the Point B. The wave directions are southward for all the points except Points B and C. These results demonstrate that Santa Catalina Island acts as a barrier and blocks wave propagation on the lee side of the island, resulting in decrease in wave height in that area.

The presence of Santa Catalina Island also induces the spread of energy, thus changing the wave spectrum. The energy balance equation of the present SWAN model solves directional wave spectrum with discrete 24 directions and 25 frequency bands. Figures 14 and 15 show the influence of the Santa Catalina Island sheltering effect on the wave energy distribution.

Figure 14 displays the directional wave spectrum at the six points (red triangles in the Figure 1) surrounding Santa Catalina Island derived from the SWAN model for 14 January 2011 at 15:00 UTC. The directional wave spectrum at Point A (Figure 14a), which is located on the upwind side of the island, shows a bimodal spectrum, and the energy density is stronger than the other points. Two wind wave systems are present at Point A, while Points B (Figure 14b) and C (Figure 14c) exhibit only single component wind waves.

In the frequency wave spectra plot shown in Figure 15, the spectra at Points A, B, and C are characterized by a single peak, which exhibits dominance of the prevailing wind wave component. The swell energy is basically dissipated at Points B and C. On the other hand, Points D, E, and F are characterized by two peaks and the swell wave is the dominant component. These figures indicate that the wave energy at Points A, E, and F on the windward side is larger than those on the lee side. The energy of the wave spectrum at the three points (B, C, and D) in the sheltered areas is small. More importantly, the spectral directions at Points B and C are largely altered to the southeastward, consistent with Figure 14. These results demonstrate that the islands in the SCB play an important role in the dissipation of wave spectrum energy and diffractive directional modifications.

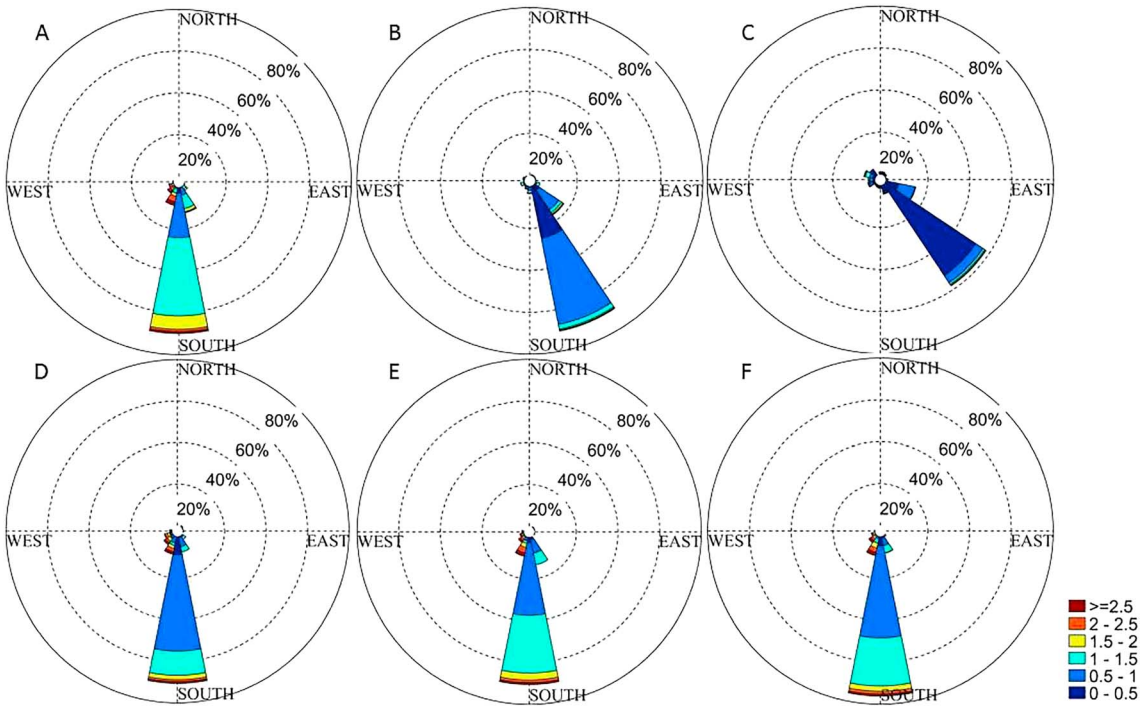

Figure 13. Mean wave direction roses around Santa Catalina Island derived from Simulating WAves Nearshore simulation for January 2011 at the six points marked by red triangles shown in Figure 1. The range of H_{sign} (units: m) is represented by the different colors shown in the legend.

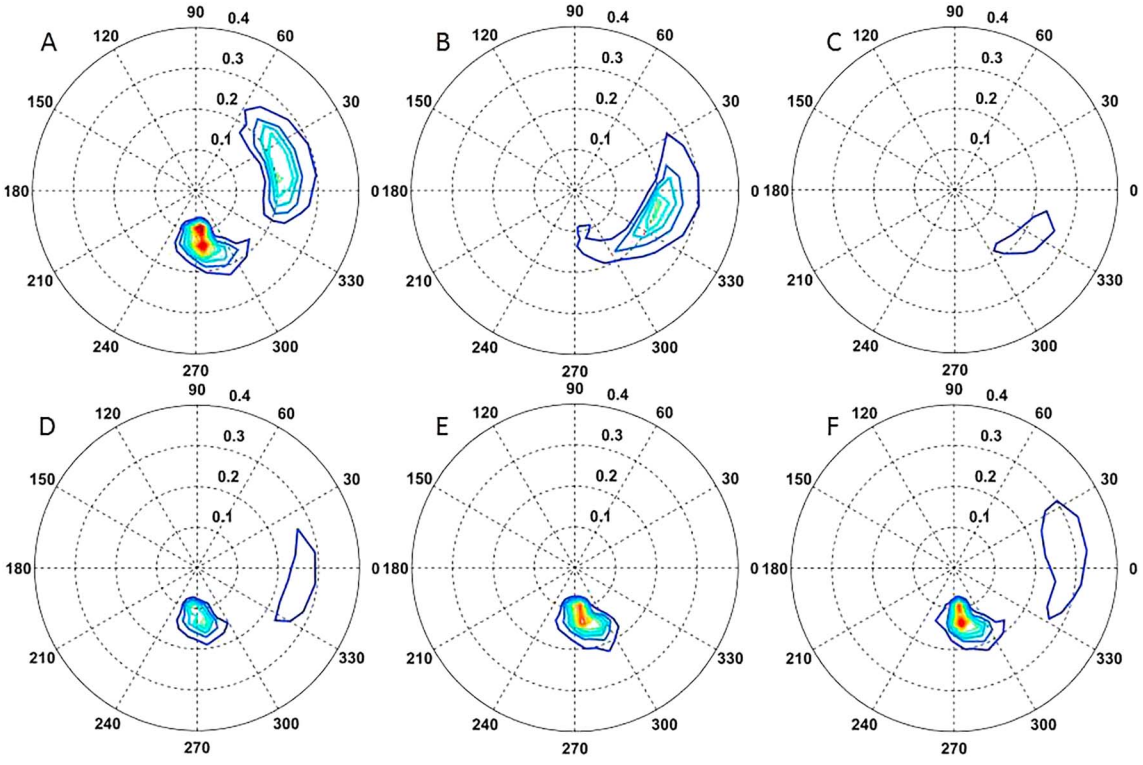

Figure 14. Directional wave spectra derived from Simulating WAves Nearshore model for 14 January 2011 at 1500 UTC at the locations marked by yellow triangles in Figure 1. The circles indicate the wave frequency from the center out with 0.2-Hz intervals.

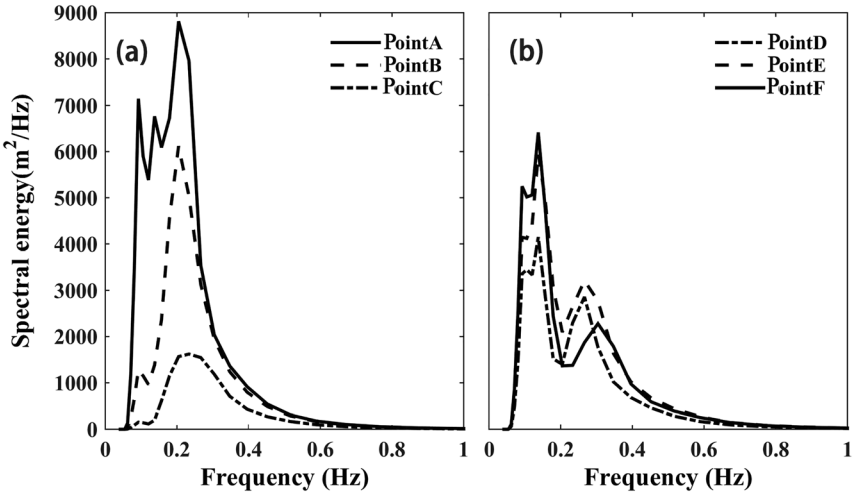

Figure 15. Frequency spectra derived from the Simulating WAves Nearshore model for 14 January 2011 at 15:00 UTC at the six locations marked by red triangles in Figure 1.

5.2. Current Effects on Waves

To investigate the effect of oceanic currents on waves, the hourly background currents with the 1-km horizontal resolution are employed in the SWAN model obtained from the Regional Ocean Modeling System simulation (Dong et al., 2009, 2012).

Oceanic current effects play roles in ocean waves generation, propagation and dissipation, which are summarized as follows: (a) when the current and wave are in the same (opposite) direction, the relative wave height will decrease (increase; Rusu & Soares, 2011; Tolman, 1991, 2010); (b) imposed additional currents (waves) affect bottom friction coefficient of the waves (currents; Mao & Xia, 2018). For instance, waves collocating with the background currents have more bottom friction and thus have a more significant impact near the shore (Signell et al., 1990); (c) and wave frequency shifts by the background current due to Doppler Effect. Uchiyama et al. (2009) discuss the important feedback effects of surf zone littoral current on the waves with emphases on Doppler shift by currents, changes in wave-averaged surface elevation in the wave dispersion relation, and the variation of Reynolds stress associated with turbulent littoral currents, due to the wave-current interaction. (Rusu & Soares, 2011). In the SWAN model, the evolution of the action density N is governed by the action balance equation (Chiang, 1983; Booij et al., 1999; Komen et al., 1994):

$$\frac{\partial N}{\partial t}+\nabla_{\vec{x}}\cdot\left[\left(\boldsymbol{c}_g+\boldsymbol{u}_c\right)N\right]+\frac{\partial c_\sigma N}{\partial \sigma}+\frac{\partial c_\theta N}{\partial \theta}=\frac{S_{tot}}{\sigma} \tag{4}$$

where $\boldsymbol{u}_c$ is the ambient current and $\boldsymbol{c}_g = \partial\sigma/\partial\boldsymbol{k}$ is the group velocity. For linear waves, dispersion relation is$\sigma^2 = g|\boldsymbol{k}|\tanh(|\boldsymbol{k}|d)$. The second term in the left hand side of equation (4) combines the group velocity and background current velocity to represent the effect of shifting the radian frequency due to variations in depth and mean currents. Hence, this term represents depth- and current-induced wave refraction. Figure 16a shows a typical example of wave energy variation under the influence of background current where wave energy$E = {}^1/_{16}\left(\rho g H_{\text{sign}}^2\right)$. From Figure 16a, one can see that the values of the energy difference ratio on the northern side of Santa Rosa Island and the southwest side of Santa Catalina Island, where cyclonic eddies are presented, are larger than offshore. Near the Santa Rosa Island, the values of energy difference ratio are positive where the angle between waves and currents is greater than 90°. However, on the upwind side and the northside of Santa Rosa Island, the angle between waves and currents is less than 45°, which leads to negative values of energy difference ratio. Therefore, the southeastward California Current, the northwestward Counter Current, topographically influenced currents behind islands and headlands, and other ambient currents have a significant impact on changing wave energy in the SCB.

In order to diagnose gross effects of currents on alteration of wave energy, the Doppler shift and current-induced advection are considered. The absolute radian frequency ω is given by the sum of the relative

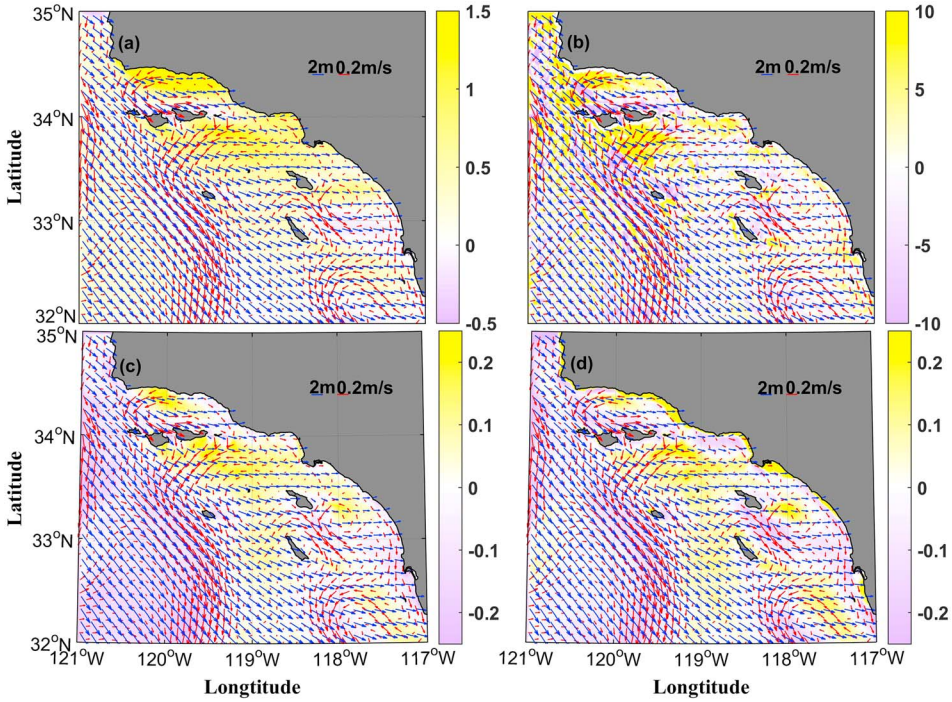

Figure 16. Normalized differences of the wave energy (shaded; units: J) between the two cases with current effects included and wave-only for July 2011 (a). Sum of $(uE)_x$ and $(vE)_y$ terms in the equation (5) (shaded; units: w) is calculated for July 2011 (b). Normalized differences of the source terms (c: energy generation; d: energy dissipation; unit: W/m^2) derived from model data between the wave-current interaction for the two cases with current effects included and only-wave-only for July 2011. The blue and red arrows represent the direction of the wave and current, respectively.

radian frequency σ, and the multiplication of the wavenumber $\boldsymbol{k}$ and ambient current velocity vector $\boldsymbol{u}_c = (u, v)$, given by the formula for Doppler shift:$\omega = \sigma + k_1 u + k_2 v$. According to equation (2), the variations of wave growth by wind and total wave dissipation due to the current effects are calculated in Figures 16c and 16d. Overall, the spatial patterns of wave generation and dissipation are closely correlated with Figure 16a.

For narrow-banded random and breaking waves, Jie and Slinn (2003) employed the following expression:

$$E_t + \left[(u + C_{g1})E\right]_x + \left[(v + C_{g2})E\right]_y + S_{11}u_x + \frac{1}{2}S_{12}(u_y + v_x) + S_{22}v_y = -\varepsilon_b \quad (5)$$

where ε_b is the ensemble-averaged dissipation function, u and v are the current velocity components in the x and y directions, and S_{ij} (i,j = 1, 2) is the wave radiation stress tensor. The spectrally integrated form of the wave energy balance equation (5) is useful to diagnose gross effects of currents on alteration of wave energy, because the interaction terms (i.e., the three last terms on the left-hand side) collectively representing work done by radiation stress S_{ij} are exposed (e.g., Jie & Slinn, 2003). $(uE)_x$ and $(vE)_y$ are current-induced advection of wave energy in the current effects. In other words, they collectively represent divergence and convergence of wave energy associated with the background currents. It is worth noting that the sum of these two terms (we call the convergence term) is found to have the largest magnitude among the other terms and is 4–5 times as large as the sum of the three radiation stress terms. Figure 16b shows the convergence term for July 2011. The pattern of the convergence terms is approximately identical to that of wave energy variation (Figure 16a).

6. Summary

The wind-generated wave plays an important role in the air-sea interaction. The multiple-scale variation is an essential part for the wave dynamics. Exploration of multiple-scale wave variations is important for us to better understand the wave dynamics and the physical processes in the upper ocean. Using numerical wave

model and observation data, the spatial and temporal variability of the wave field in the SCB is investigated. The temporal multiple scales are presented in the wave field: interannual, seasonal, intraseasonal, and diurnal. Seasonal variation is the most prominent in the SCB wave variability. The maximum values of H_{sign}, H_{swell}, and the wave peak period occur during winter and the minimum in summer. ENSO events have footprints on the wave interannual variation. The intraseasonal events can be detected. The diurnal cycle is due to the land-sea breeze.

The effects of island sheltering and currents on waves are discussed. The eight islands located in the SCB cause refraction and diffraction, resulting in the wave height to decrease and the wave direction to change in lee sides of islands. Due to the sheltering effect of the islands, the impact of waves on the southern California coast is greatly reduced. The detailed diagnosis reveals that the wave energy convergence associated with background currents is responsible for altering the waves in the SCB, with coincident modification of the wind input and wave dissipation.

Acknowledgments

This study is supported by the National Key Research and Development Program of China (2016YFC1401407) and the Natural Science Foundation of Jiangsu Higher Education Institution of China (16KJB170011). C. D. appreciates the support from the National Key Research and Development Program of China (2017YFA0604100), the National Program on Global Change and Air-Sea Interaction (GASI-03-IPOVAI-05), the National Key Research and Development Program of China (2016YFA0601803), the National Natural Science Foundation of China (41476022 and 41490643), the Startup Foundation for Introducing Talent of Nanjing University of Information Science and Technology (2014r072), Program for Innovation Research and Entrepreneurship team in Jiangsu Province, the Bureau of Ocean Energy Management Environmental Studies Program (M14AC00021), the Japan Society for the Promotion of Science (JSPS) Grant-in-aid for Scientific Research (15H04049, 15KK0207, and 18H03798), the Public science and technology research funds projects of ocean (201505013), and the Postgraduate Research & Practice Innovation Program of Jiangsu Province (KYCX18_1020). The buoy data are downloaded from https://www.ndbc.noaa.gov maintained by the National Data Buoy Center.

References

Adams, P. N., Inman, D. L., & Graham, N. E. (2008). Southern California deep-water wave climate: Characterization and application to coastal processes. *Journal of Coastal Research*, *24*(4), 1022–1035. https://doi.org/10.2112/07-8031.1

Adams, P. N., Inman, D. L., & Lovering, J. L. (2011). Effects of climate change and wave direction on longshore sediment transport patterns in Southern California. *Climatic Change*, *109*(S1), 211–228. https://doi.org/10.1007/s10584-011-0317-0

Amante, C., & Eakins, B. W. (2009). Etopo1 1 arc-minute global relief model: procedures, data sources and analysis. *Psychologist*, *16*(3), 20–25. https://doi.org/10.7289/V5C8276M

Arthur, & Siple, R. (1951). The effect of islands on surface waves. Scripps Institution of Oceanography. https://escholarship.org/uc/item/9sz6r0qc

Battjes, J. A., & Janssen, J. P. F. M. (1978). Energy loss and set-up due to breaking of random waves. *Coastal Engineering*, 569–587. https://doi.org/10.9753/icce.v16.

Booij, N., Holthuijsen, L., & Battjes, J. (2001). Ocean to near-shore wave modelling with SWAN. *Conference on Coastal Dynamics*, 335–344. https://doi.org/10.1061/40566(260)34

Booij, N., Ris, R. C., & Holthuijsen, L. H. (1999). A third-generation wave model for coastal regions: 1. Model description and validation. *Journal of Geophysical Research. Oceans*, *104*, 7649–7666. https://doi.org/10.1029/98JC02622

Chiang, C. M. (1983). *The applied dynamics of ocean surface waves*. Singapore: Wiley. https://doi.org/10.1142/0752

Collins, J. I. (1972). Prediction of shallow-water spectra. *Journal of Geophysical Research*, *77*, 2693–2707. https://doi.org/10.1029/JC077i015p02693

Crosby, S. C., O'Reilly, W. C., & Guza, R. T. (2016). Modeling long-period swell in Southern California: Practical boundary conditions from buoy observations and global wave model predictions. *Journal of Atmospheric and Oceanic Technology*, *33*(8), 1673–1690. https://doi.org/10.1175/JTECH-D-16-0038.1

Dee, D. P., Uppala, S. M., Simmons, A. J., Berrisford, P., Poli, P., Kobayashi, S., Andrae, U., et al. (2011). The era-interim reanalysis: Configuration and performance of the data assimilation system. *Quarterly Journal of the Royal Meteorological Society*, *137*(656), 553–597. https://doi.org/10.1002/qj.828

Dong, C., Idica, E. Y., & Mcwilliams, J. C. (2009). Circulation and multiple-scale variability in the Southern California Bight. *Progress in Oceanography*, *82*(3), 168–190. https://doi.org/10.1016/j.pocean.2009.07.005

Dong, C., Lin, X., Liu, Y., Nencioli, F., Chao, Y., Guan, Y., Chen, D., et al. (2012). Three-dimensional oceanic eddy analysis in the Southern California Bight from a numerical product. *Journal of Geophysical Research*, *117*, C00H14. https://doi.org/10.1029/2011JC007354

Eshleman, J. L., Barnard, P. L., Li, H. E., & Hanes, D. M. (2005). Coupling alongshore variations in wave energy to beach morphologic change using the swan wave model at ocean beach, San Francisco, CA. *Center for Integrated Data Analytics Wisconsin Science Center*.

Group, & W, T. (1988). The WAM model—A third generation ocean wave prediction model. *Journal of Physical Oceanography*, *18*(12), 1775–1810. https://doi.org/10.1175/1520-0485(1988)018<1775:TWMTGO>2.0.CO;2

Hasselmann, K. (1973). Measurements of wind-wave growth and swell decay during the joint North Sea wave project (JONSWAP). *Dtsch. hydrogr.z*, *12*(2), 1–95.

Hasselmann, K. (1974). On the spectral dissipation of ocean waves due to white capping. *Boundary-Layer Meteorology*, *6*(1–2), 107–127. https://doi.org/10.1007/BF00232479

Hasselmann, S., Hasselmann, K., Allender, J. H., & Barnett, T. P. (1985). Computations and parameterizations of the nonlinear energy transfer in a gravity wave spectrum. Part II: Parameterizations of the nonlinear transfer for application in wave models. *Journal of Physical Oceanography*, *15*(11), 1378–1391. https://doi.org/10.1175/1520-0485(1985)015<1378:CAPOTN>2.0.CO;2

Hasselmann, S., Hasselmann, K., Bauer, E., Janssen, P. A. E. M., & Ewing, J. A. (1988). The WAM model - A third generation ocean wave prediction model. *Journal of Physical Oceanography*, *18*, 1775–1810. http://doi.org/10.1175/1520-0485(1988)018<1775:TWMTGO>2.0.CO;2

Holthuijsen, L. H., Herman, A., & Booij, N. (2003). Phase-decoupled refraction–diffraction for spectral wave models. *Coastal Engineering*, *49*(4), 291–305. https://doi.org/10.1016/S0378-3839(03)00065-6

Hughes, M., Hall, A., & Fovell, R. G. (2007). Dynamical controls on the diurnal cycle of temperature in complex topography. *Climate Dynamics*, *29*(2-3), 277–292. https://doi.org/10.1007/s00382-007-0239-8

Jie, Y., & Slinn, D. N. (2003). Effects of wave-current interaction on rip currents. *Journal of Geophysical Research*, *108*(C3), 3088. https://doi.org/10.1029/2001JC001105

Komen, G. J., Cavaleri, L., Donelan, M., Hasselmann, K., Hasselmann, S., & Janssen, P. A. E. M. (1994). Dynamics and modelling of ocean waves. *Dynamics of Atmosphere and Oceans*, *25*(4), 276–278.

León, S. P. D., & Soares, C. G. (2005). On the sheltering effect of islands in ocean wave models. *Journal of Geophysical Research*, *110*, C09020. https://doi.org/10.1029/2004JC002682

León, S. P. D., & Soares, C. G. (2010). The sheltering effect of the Balearic Islands in the hindcast wave field. *Ocean Engineering*, *37*(7), 603–610. https://doi.org/10.1016/j.oceaneng.2010.01.011

Madsen, O. S., Poon, Y. K., & Graber, H. C. (1988). Spectral wave attenuation by bottom friction: Theory. *International Conference on Coastal Engineering*, *45*, 492–504. https://doi.org/10.1061/9780872626874.035

Mao, M., & Xia, M. (2018). Wave-current dynamics and interactions near the two inlets of a shallow lagoon-inlet-coastal ocean system under hurricane conditions. *Ocean Modelling*, *129*, 124–144. https://doi.org/10.1016/j.ocemod.2018.08.002

Miles, J. W. (1960). On the generation of surface waves by shear flows. *Journal of Fluid Mechanics*, *3*(02), 185–204. https://doi.org/10.1017/S0022112057000567

O'Reilly, W. C., & Guza, R. T. (1993). A comparison of two spectral wave models in the Southern California Bight. *Coastal Engineering*, *19*(3–4), 263–282. https://doi.org/10.1016/0378-3839(93)90032-4

O'Reilly, W. C., R. T. Guza, & R. J. Seymour (1999). Wave prediction in the Santa Barbara channel, in *Proceedings of the 5th California Islands Symposium*, pp. 76–80, Min. Manage. Serv., Santa Barbara, Calif.

O'Reilly, W. C., Olfe, C. B., Thomas, J., Seymour, R. J., & Guza, R. T. (2016). The California coastal wave monitoring and prediction system. *Coastal Engineering*, *116*, 118–132. https://doi.org/10.1016/j.coastaleng.2016.06.005

Pawka, S. S., Inman, D. L., & Guza, R. T. (1984). Island sheltering of surface gravity waves: Model and experiment. *Continental Shelf Research*, *3*(1), 35–53. https://doi.org/10.1016/0278-4343(84)90042-6

Phillips, O. M. (1957). On the generation of waves by turbulent wind. *Journal of Fluid Mechanics*, *2*(05), 417–445. https://doi.org/10.1017/S0022112057000233

Remya, P. G., & Kumar, R. (2013). Impact of diurnal variation of winds on coastal waves off south east coast of India. *International Journal of Ocean & Climate Systems*, *4*(3), 171–179. https://doi.org/10.1260/1759-3131.4.3.171

Renault, L., Hall, A., & Mcwilliams, J. C. (2016). Orographic shaping of us west coast wind profiles during the upwelling season. *Climate Dynamics*, *46*(1–2), 273–289. https://doi.org/10.1007/s00382-015-2583-4

Rogers, W. E., Kaihatu, J. M., Hsu, L., Jensen, R. E., Dykes, J. D., & Holland, K. T. (2007). Forecasting and hindcasting waves with the swan model in the Southern California Bight. *Coastal Engineering*, *54*(1), 1–15. https://doi.org/10.1016/j.coastaleng.2006.06.011

Rusu, L., & Soares, C. G. (2011). Modelling the wave–current interactions in an offshore basin using the swan model. *Ocean Engineering*, *38*(1), 63–76. https://doi.org/10.1016/j.oceaneng.2010.09.012

Saha, U., Siingh, D., Midya, S. K., Singh, R. P., Singh, A. K., & Kumar, S. (2017). Spatio-temporal variability of lightning and convective activity over South/Southeast Asia with an emphasis during El Niño and La Niña. *Atmospheric Research*, *197*, 150–166. https://doi.org/10.1016/j.atmosres.2017.07.005

Seymour, R. (1996). Wave climate variability in Southern California. *Journal of Waterway, Port, Coastal, and Ocean Engineering*, *122*(4), 182–186. https://doi.org/10.1061/(ASCE)0733-950X(1996)122:4(182)

Seymour, R. J., Strange III, R. R., Cayan, D. R., & Nathan, R. A. (1985). Influence of El Niño's on California's wave climate. In Coastal Engineering 1984 (pp. 577–592).

Signell, R. P., Beardsley, R. C., Graber, H. C., & Capotondi, A. (1990). Effect of wave-current interaction on wind-driven circulation in narrow, shallow embayments. *Journal of Geophysical Research*, *95*, 9671–9678. https://doi.org/10.1029/JC095iC06p09671

Storlazzi, C. D., & Griggs, G. B. (2000). Influence of El Niño–Southern Oscillation (ENSO) events on the evolution of central California's shoreline. *Geological Society of America Bulletin*, *112*(2), 236–249. https://doi.org/10.1130/0016-7606(2000)112<236:IOENOE>2.0.CO;2

Tolman, H. L. (1991). A third-generation model for wind waves on slowly varying, unsteady, and inhomogeneous depths and currents. *Journal of Physical Oceanography*, *21*(6), 782–797. https://doi.org/10.1175/1520-0485(1991)021<0782:ATGMFW>2.0.CO;2

Tolman, H. L. (2010). The influence of unsteady depths and currents of tides on wind-wave propagation in shelf seas. *Journal of Physical Oceanography*, *20*(8), 1,166–1,174. https://doi.org/10.1175/1520-0485(1990)020<1166:TIOUDA>2.0.CO;2

Uchiyama, Y., Mcwilliams, J. C., & Restrepo, J. M. (2009). Wave-current interaction in nearshore shear instability analyzed with a vortex force formalism. *Journal of Geophysical Research*, *114*, C06021. https://doi.org/10.1029/2008JC005135

Xu, J. P., & Noble, M. A. (2009). Variability of the Southern California wave climate and implications for sediment transport. *Special Paper of the Geological Society of America*, *454*, 171–191. https://doi.org/10.1130/2009.2454(3.2)

Young, I. R., Zieger, S., & Babanin, A. V. (2011). Global trends in wind speed and wave height. *Science*, *332*(6028), 451–455. https://doi.org/10.1126/science.1197219

Yuan, Y., Yang, H., & Chongyin, L. (2012). Study of El Niño events of different types and their potential impact on the following summer precipitation in China. *Acta Meteorologica Sinica (in Chinese)*, *70*(3), 467–478.

Erratum

In the originally published version of this article, Figure 12 was incorrectly published with same image as Figure 11. This error has been corrected, and this may be considered the official version of record.